

Improving Direct Physical Properties Prediction of Heterogeneous Materials from Imaging Data via Convolutional Neural Network and a Morphology-Aware Generative Model

Ruijin Cang^{a,*}, Hechao Li^{b,*}, Hope Yao^a, Yang Jiao^b, Yi Ren^{a,**}

^a*Mechanical Engineering, Arizona State University, Tempe*

^b*Material Science and Engineering, Arizona State University, Tempe*

Abstract

Direct prediction of material properties from microstructures through statistical models has shown to be a potential approach to accelerating computational material design with large design spaces. However, statistical modeling of highly nonlinear mappings defined on high-dimensional microstructure spaces is known to be data-demanding. Thus, the added value of such predictive models diminishes in common cases where material samples (in forms of 2D or 3D microstructures) become costly to acquire either experimentally or computationally. To this end, we propose a generative machine learning model that creates an arbitrary amount of artificial material samples with negligible computation cost, when trained on only a limited amount of authentic samples. The key contribution of this work is the introduction of a morphology constraint to the training of the generative model, that enforces the resultant artificial material samples to have the same morphology distribution as the authentic ones. We show empirically that the proposed model creates artificial samples that better match with the authentic ones in material property distributions than those generated from a state-of-the-art Markov Random Field model, and thus is more effective at improving the prediction performance of a predictive structure-property model.

Keywords: Structure-Property Mapping, Integrated Computational Material Engineering, Deep Learning, Generative Model

1. Introduction

Direct prediction of material properties through predictive models has attracted interests from both material and data science communities. Predictive models have the potential to mimic highly nonlinear physics-based mappings, thus reducing dependencies on numerical

*Equal contribution

**Corresponding author

Email addresses: cruijin@asu.edu (Ruijin Cang), hechaoli@asu.edu (Hechao Li), houpuyao@asu.edu (Hope Yao), yjiao13@asu.edu (Yang Jiao), yiren@asu.edu (Yi Ren)

URL: designinformatics.github.io (Yi Ren)

simulations or experiments during material design, and enabling tractable discovery of novel yet complex material systems [1, 2, 3]. Nonetheless, the construction of predictive models for nonlinear functions, such as material structure-property mappings, is known to be data-demanding, especially when the inputs, e.g., material microstructures represented as 2D or 3D images, are high-dimensional [4]. Thus, the added value of predictive models quickly diminishes as the acquisition cost increases for material samples. We investigate in this paper a computational approach to generate artificial material samples with negligible cost, by exploiting the fact that all samples within one material system share similar morphology. More concretely, we define morphology as a style vector quantified from a microstructure sample, and propose a generative model that learns from a small set of authentic samples, and creates an arbitrary amount of artificial samples that share the same distribution of morphologies as the authentic ones.

The key contribution of the paper is the introduction of a morphology constraint on the generative model that significantly improves the morphological consistency between the artificial and authentic samples from benchmark generative models. To demonstrate the utility of the proposed model, we run a case study on the prediction of the Young’s modulus, the diffusion coefficient and the permeability coefficient of sandstone microstructures. We show that the generated artificial samples from the proposed model can improve the prediction performance more effectively than those from a state-of-the-art Markov Random Field (MRF) model.

As an overview, the proposed model follows the architecture of a variational autoencoder [5] that learns to encode material microstructures into a lower-dimensional latent space and to decode samples from the latent space back into microstructures. Both the encoder and the decoder are composed of feed-forward convolutional neural networks for extracting and generating local morphological patterns, and are jointly trained to minimize the discrepancy between the artificial and authentic samples. The target morphology is quantified from the authentic samples by an auxiliary network. The idea of quantifying material morphology through a deep network is inspired by the style transfer technique originally developed for image synthesis [6].

The rest of the paper is structured as follows: In Sec. 2 we review related work on material representations and reconstruction, based on which we delineate the novelty of this paper. We then introduce background knowledge on variational autoencoder and style transfer. Sec. 3 elaborates on the details of the proposed model. Sec. 4 presents a case study on the prediction of sandstone properties, where we demonstrate the superior performance of the proposed model against the benchmarks, in both microstructure generation, and the resultant property prediction accuracy. In Sec. 5 we summarize findings from the case study and propose potential future directions. Sec. 6 concludes the paper.

2. Background

2.1. Data science challenges in computational material science

Incorporating data science into material discovery [1] and design [7] faces unique challenges with high dimensionality of material representations and the lack of material data

due to high acquisition costs. We review existing work that address these challenges to some extent.

Challenge 1: Mechanisms for understanding material representations. A common approach to addressing the issue of high dimensionality is to seek for a representation, i.e., an encoder-decoder pair, for a material system: The encoder transforms microstructures to their reduced representations, and the decoder generates (i.e., reconstructs) them back from their representations. A good encoder-decoder pair should both achieve significant dimension reduction, and good matching between the data distribution (i.e., the distribution of authentic samples) and the model distribution (i.e., the distribution defined by the decoder). This is often feasible for material systems with consistent and quantifiable morphologies among their samples, as reviewed below.

Existing encoders for material representations can be categorized as physical and statistical, some of which have led to accelerated design of various material systems [8, 9, 10, 11, 12]. Among all, **physical encoders** characterize microstructures using composition (e.g., the percentage of each material constituent) [13, 14], dispersion (e.g., inclusions' spatial relation, pair correlation, the ranked neighbor distance [15, 16, 17, 18, 19, 20]), and geometry features (e.g., the radius/size distribution, roundness, eccentricity, and aspect ratio of elements of the microstructure [17, 15, 8, 21, 22, 23, 24, 25]). Among **statistical encoders** are the N-point correlation functions [26, 18, 8, 21, 22]. Torquato et al. [27, 28, 8] show that the microstructure of heterogeneous materials can be characterized statistically via various types of N-point correlation functions [29, 30]. Similar descriptors include lineal path function [31] and statistics calculated based on the frequency domain using fast Fourier transformation [32, 33]. Another type of statistical encoders are **random fields** [34, 35, 36], which define joint probability functions on the space of microstructures. Typical probability models include Gaussian random fields [37, 38, 8] which treats binary microstructure images as level sets, and Markov random fields, where each pixel of the microstructure is assumed to be drawn from a probability function conditioned on its neighbouring pixels [35].

Decoding of representations, i.e., generation of microstructure through existing physical and statistical representations, involves optimization in the microstructure space: For physical representations and N-point correlation functions, a microstructure is searched to minimize its difference from the target descriptors. For random fields, the generation can be done by maximizing the joint probability through Markov chain Monte Carlo simulations [35, 36]. While it is shown that material generation through these representations is feasible [18, 22, 8, 11], the computational costs for the optimization through gradient [32, 11] and non-gradient [28, 39, 40, 41] methods are often high.

In addition to the difficulties in decoding, the existing encoders are not universally applicable, especially to material systems with complex morphology. More specifically, matching in the representation space does not guarantee the match in the microstructure space. An example can be found in Fig. 1, where we compare two-point correlation functions of Ti64 alloy samples and three sets of artificial images (see details from [35, 42, 43]). The visually more plausible set has worse match to the target with respect to the Euclidean distance in the discretized 2-point correlation space.

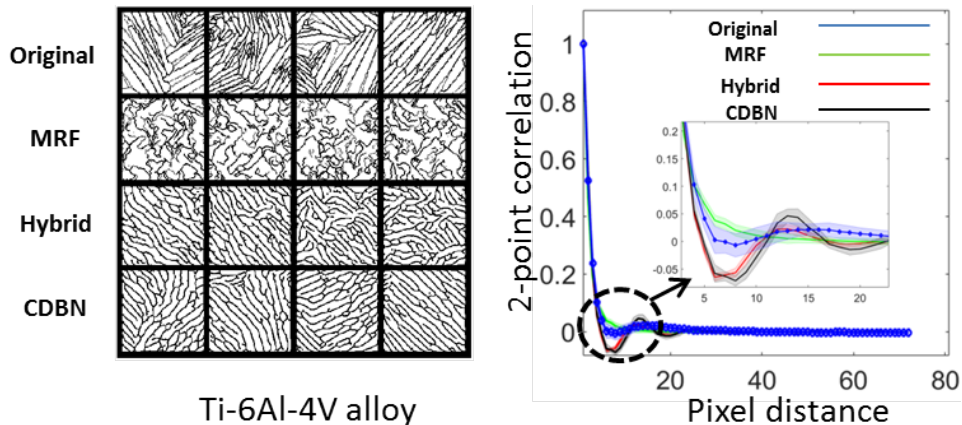


Figure 1: Comparison of two-point correlation functions among four sets of images. From left to right: Authentic microstructure samples, samples generated by a Markov random field model [35], samples generated by a hybrid model with deep belief network and Markov random field [43], and samples generated by a deep belief network [42]. Better matching in the discretized 2-point correlation space does not indicate better microstructure generations.

These existing difficulties leads to the need for new mechanisms to define material representations. We propose four metrics for evaluating the utility of a material representation: interpretability, dimensionality, expressiveness, and generation cost: Physical descriptors and correlation functions are designed to be interpretable and relatively low dimensional, yet may not be expressive enough to capture complex morphologies and requires optimization during generation; random fields are relatively expressive (and some permit fast generation [35]), but are often high-dimensional and less interpretable. Both categories of representations are material specific, i.e., new representations need to be manually identified for new material systems. Cang et al. [42] proposed to learn statistical generative models from microstructures to automatically derive expressive, low dimensional representations that enables fast microstructure generation. They showed that a particular type of generative model, called Convolutional Deep Belief Network (CDBN) [44], can produce reasonable microstructures for material systems with complex morphologies, by extracting morphology patterns at different length scales from samples, and decode an arrangement of these patterns (the hidden activation of the network) back into a microstructure. Nonetheless, CDBNs are trained layer-by-layer, and thus require additional material-dependent parameter tuning to achieve plausible generations.

Different from [42], this paper proposes a model that directly enforces the matching of the artificial microstructures to the authentic ones, thus avoiding additional parameter tuning. Our model is also fully differentiable, making it much easier to train than CDBNs and scalable to deep architectures. Lastly, the introduction of the morphology constraint further refines the artificial microstructures under a small amount of training data. With all these improvements, the proposed model is generally applicable to the extraction of low dimensional material representations, and is expressive for generating microstructures with morphologies of decent complexity.

Challenge 2: Effective material data acquisition methods. Unlike scenarios in contemporary machine learning where a large quantity of data is available, in computational material design tasks we may only have a limited amount of microstructure and property samples, and the acquisition cost for additional samples is usually high. This challenge calls for the incorporation of active learning methods into the design. The key idea of active learning is to minimize the data acquisition cost for learning a model (e.g., generative models for capturing microstructure distributions, or discriminative models for predicting process-structure-property mappings), by optimally controlling the balance between data exploitation and exploration [45, 46]. In computational material science, such techniques have been adopted to accelerate the process of material discovery for desired properties [47, 48]. While this paper does not focus directly on active learning, we demonstrate that the quality of the microstructure data, along with its quantity, can significantly influence the prediction performance of a statistical structure-property mapping, and thus justify the value of the proposed generative model.

2.2. Preliminaries on predictive and generative models

This paper will involve three networks: The generative network for creating artificial material microstructures, the auxiliary convolutional network for quantifying material morphologies, and another convolutional network for structure-property prediction. We provide technical backgrounds for these models below.

Generation through Variational Autoencoder. Variational autoencoders (VAE) [5] are extensions of autoencoders [49]. An autoencoder (Fig. 2a) is composed by two parts: an encoder $\mathbf{z} = f(\mathbf{x})$ converts the input \mathbf{x} to a hidden vector \mathbf{z} , and a decoder produces a reconstruction $\hat{\mathbf{x}} = g(\mathbf{z})$. An AE is trained to minimize the discrepancy between inputs \mathbf{x} and their corresponding reconstructions $\hat{\mathbf{x}}$. Variants of autoencoders (e.g., Sparse [50], denoising [51], and contractive [52]) have been proposed to improve the learning of more concise representations from high-dimensional input data, and are widely used for data compression [53], network pre-training [54], and feature extraction [55]. However, conventional autoencoders are prone to generating implausible new outputs, see Fig. 7b for examples, as they do not attempt to match the model distribution (the distribution of images generated from the decoder) with the data distribution (the distribution of input images). VAE (Fig. 2b) was introduced to address this issue [5], by constraining the distribution of the latent variables \mathbf{z} encoded from the input data to that used for output generation, thus indirectly forcing the match between the distributions of the model outputs and the data.

The VAE model. We start with the decoder, which defines the output distribution, $p_{\theta}(\mathbf{x}|\mathbf{z})$, conditioned on the latent vector \mathbf{z} , and is parameterized by θ . Let the input data be $\mathcal{X} = \{\mathbf{x}_i\}_{i=1}^N$, which defines a data distribution $p(\mathbf{x})$, and let $p(\mathbf{z})$ be the pre-specified sampling distribution in the latent space. The goal is to train a model that matches the marginal distribution $p_{\theta}(\mathbf{x})$ to the data distribution $p(\mathbf{x})$. In the following, we show that this is indirectly achieved by matching the posterior $p_{\theta}(\mathbf{z}|\mathbf{x})$ to $p(\mathbf{z})$.

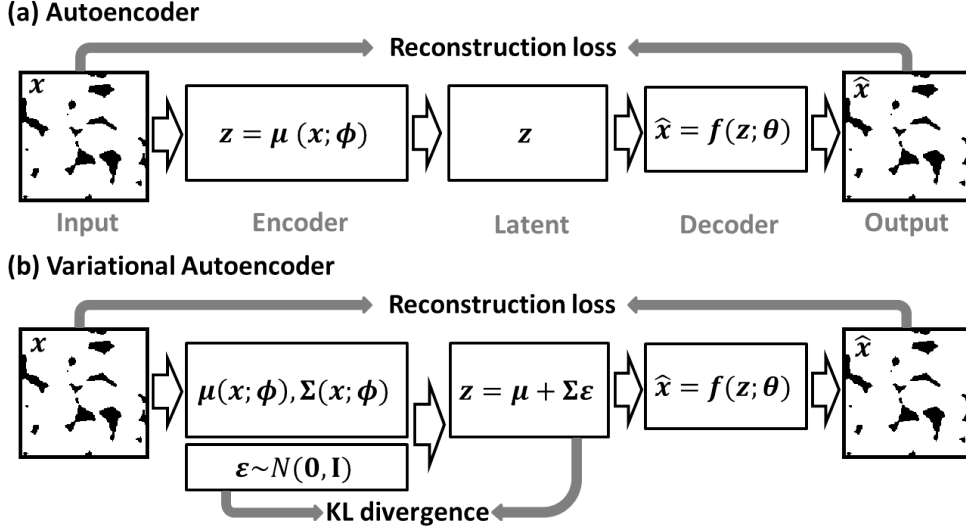


Figure 2: (a) An autoencoder converts inputs to a latent space and reconstructs outputs from samples in the latent space. It is trained to minimize the reconstruction error. (b) A variational autoencoder converts inputs to a distribution in the latent space. It is trained to minimize both the reconstruction error and the Kullback-Leibler (KL) divergence between the latent distribution and a sample distribution (often standard normal).

First, the marginal is defined as

$$p_{\theta}(\mathbf{x}) = \int_{\mathbf{z}} p_{\theta}(\mathbf{x}|\mathbf{z})p(\mathbf{z})d\mathbf{z} = E_{\mathbf{z}\sim p(\mathbf{z})}p_{\theta}(\mathbf{x}|\mathbf{z}). \quad (1)$$

Matching the model and data distributions requires maximizing the likelihood $\prod_{\mathbf{x}\in\mathcal{X}}p_{\theta}(\mathbf{x})$ with respect to θ . This maximization problem, however, is often intractable due to the numerical integral and the complexity of the decoder network. Nonetheless, it is noted that for a given \mathbf{x} , most samples in the latent space will have $p_{\theta}(\mathbf{x}|\mathbf{z}) \approx 0$, as these latent samples do not generate outputs close to \mathbf{x} . This leads to the idea of introducing another distribution $q_{\phi}(\mathbf{z}|\mathbf{x})$ (the encoder) that takes an \mathbf{x} and outputs \mathbf{z} values that are likely to reproduce \mathbf{x} . Ideally, the space of \mathbf{z} that are likely under q will be much smaller than that under $p(\mathbf{z})$, making the computation of $E_{\mathbf{z}\sim q}p_{\theta}(\mathbf{x}|\mathbf{z})$ relatively cheap. However, $E_{\mathbf{z}\sim q}p_{\theta}(\mathbf{x}|\mathbf{z})$ is not the same as $p(\mathbf{x})$, as $q_{\phi}(\mathbf{z}|\mathbf{x})$ does not necessarily match to $p(\mathbf{z})$. The relation between the two is derived below.

We start by deriving the Kullback-Leibler divergence between the encoded latent distribution $q_{\phi}(\mathbf{z}|\mathbf{x})$ and the posterior $p_{\theta}(\mathbf{z}|\mathbf{x})$:

$$\begin{aligned} D_{KL}(q_{\phi}(\mathbf{z}|\mathbf{x})||p_{\theta}(\mathbf{z}|\mathbf{x})) &= \int q_{\phi}(\mathbf{z}|\mathbf{x}) \log \frac{q_{\phi}(\mathbf{z}|\mathbf{x})}{p_{\theta}(\mathbf{z}|\mathbf{x})} d\mathbf{z} \\ &= -\mathbb{E}_{\mathbf{z}\sim q}[\log p(\mathbf{z}, \mathbf{x})] - \mathbb{E}_{\mathbf{z}\sim q}[-\log q_{\phi}(\mathbf{z}|\mathbf{x})] + \log p(\mathbf{x}). \end{aligned} \quad (2)$$

By rearranging Eq. (2), we get

$$\log p(\mathbf{x}) - D_{KL}(q_{\phi}(\mathbf{z}|\mathbf{x})||p_{\theta}(\mathbf{z}|\mathbf{x})) = \mathbb{E}_{\mathbf{z}\sim q}[\log p_{\theta}(\mathbf{x}|\mathbf{z})] - D_{KL}(q_{\phi}(\mathbf{z}|\mathbf{x})||p(\mathbf{z})). \quad (3)$$

Note that the right hand side of Eq. (3) can be maximized through stochastic gradient descent: The first term $\mathbb{E}_{\mathbf{z}\sim q}[\log p_{\theta}(\mathbf{x}|\mathbf{z})]$ measures the reconstruction error, i.e., the expected difference between an input \mathbf{x} and its reconstructions drawn from the decoder conditioned on the latent variables, which are further drawn from the encoder conditioned on the input. The second term $D_{\text{KL}}(q_{\phi}(\mathbf{z}|\mathbf{x})||p(\mathbf{z}))$ measures the difference between the encoded distribution of \mathbf{z} and the modeled latent distribution $p(\mathbf{z})$. Since the encoding and decoding processes involved in these terms are modeled as feedforward networks, the gradients are readily available for backpropagation. Specifically, we model $q_{\phi}(\mathbf{z}|\mathbf{x}) = \mathcal{N}(\mathbf{z}|\boldsymbol{\mu}(\mathbf{x};\boldsymbol{\phi}), \boldsymbol{\Sigma}^2(\mathbf{x};\boldsymbol{\phi}))$ as a normal distribution parameterized by the mean $\boldsymbol{\mu}(\mathbf{x};\boldsymbol{\phi})$ and the diagonal variance matrix $\boldsymbol{\Sigma}^2(\mathbf{x};\boldsymbol{\phi})$. $\boldsymbol{\mu}$ and $\boldsymbol{\Sigma}$ are the outputs of the encoder network. We similarly model $p_{\theta}(\mathbf{x}|\mathbf{z}) = \mathcal{N}(\mathbf{x}|\mathbf{f}(\mathbf{z};\boldsymbol{\theta}), \sigma^2\mathbf{I})$ with mean $\mathbf{f}(\mathbf{z};\boldsymbol{\theta})$ and variance σ^2 . The function $\mathbf{f}(\mathbf{z};\boldsymbol{\theta})$ is the decoder network; σ determines the importance of the reconstruction of \mathbf{x} during the training of a generative model, and is set to 1 in the proposed model. The prior of the latent distribution, $p(\mathbf{z})$, is often assumed to be standard normal. This is because the transformation from this simple distribution to the potentially highly nonlinear data distribution $p(\mathbf{x})$ can often be achieved by a sufficiently deep decoder.

The left hand side of Eq. (3) contains the objective $\log p_{\theta}(\mathbf{x})$ that we want to maximize, and the KL-divergence $D_{\text{KL}}(q_{\phi}(\mathbf{z}|\mathbf{x})||p_{\theta}(\mathbf{z}|\mathbf{x})) > 0$ that should ideally reach 0. Thus, minimizing

$$L(\theta, \phi, \mathbf{x}) = -\mathbb{E}_{\mathbf{z}\sim q}[\log p_{\theta}(\mathbf{x}|\mathbf{z})] + D_{\text{KL}}(q_{\phi}(\mathbf{z}|\mathbf{x})||p(\mathbf{z})) \quad (4)$$

will maximize a lower bound of $p(\mathbf{x})$.

Prediction through Convolutional Neural Network (CNN). We build a predictive structure-property model using CNN (Sec. 3). A CNN is often composed of one or more convolutional layers followed by fully connected layers. A convolutional layer consists of a set of image filters, each as a set of network edges connecting the input image to a hidden channel, see Fig. 3. Scanning the input image with a filter requires the network weights to be shared, thus reducing the total number of weights to be trained. A max-pooling layer further reduces the dimension of a hidden layer [56].

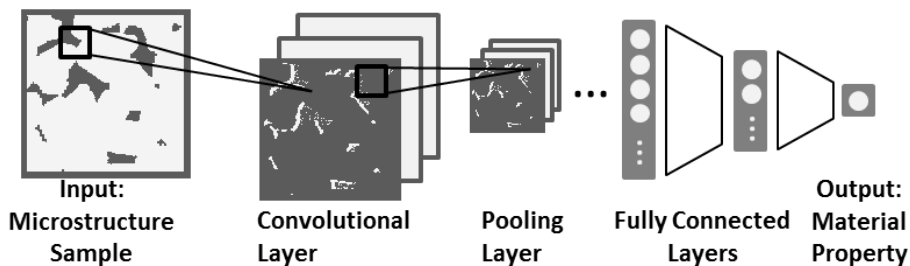


Figure 3: Schematic plot for a CNN

Style transfer (ST). ST was first introduced to integrate the content of one image with the style of another [6]. To perform ST, a “style vector” is first computed for an image, that

consists of the variance-covariance matrices of the hidden states of a pre-trained CNN (we use a VGG Net [57] in this paper) activated by the input image. A new image can then be created by minimizing the difference between its style vector and the target one. One can also preserve the image content, i.e., the hidden states of the deepest layers, by adding an additional loss on the content difference.

As will be discussed in Sec. 3, the proposed method extends ST to a generative setting, by directly adding a style (morphology) penalty to the training loss of a VAE. There are two major difference in comparison: First, the standard ST generates images by minimizing the style loss with respect to a high-dimensional image space, while our model is learned to directly generate style-consistent images, thus is significantly faster than standard ST; second, the standard ST uses a single style vector as a target, while our model can encode a distribution of styles in its latent space, and thus is more expressive as a generator.

3. Proposed Models

3.1. Network specifications

The generative model. The proposed generative model is composed of two networks, a VAE for image encoding and decoding, and an auxiliary network for computing the style vector (\mathbf{G}). See model summary in Fig. 4a. For the VAE, its encoder has convolutional layers of a fixed filter size (4×4), max-pooling layers after each other convolutional layers, and two fully-connected layers of sizes 256 and 16, respectively. Each pooling layer is of stride 2, i.e., it is composed with filters of size 2×2 applied to the hidden layers, downsampling these layers by a factor of 2 along both width and height. Together, the encoder reduces the dimension of the input from 128×128 to 16×1 . The architecture of the decoder is symmetric to that of the encoder.

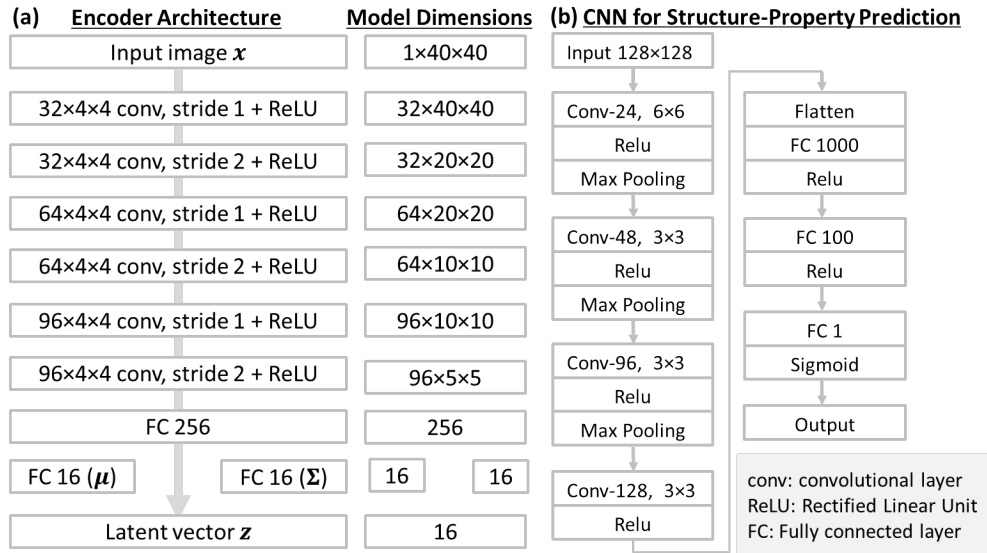


Figure 4: (a) Encoder architecture in the VAE, decoder is mirrored from the encoder (b) CNN architecture

The predictive model. A CNN is built to predict material properties from microstructures. A schematic of the predictive model is in Fig. 4b. We use four convolutional layers with filter size 3×3 , and max-pooling layers with stride 2.

The morphology style model. To acquire a rich set of morphology patterns and make this acquisition process general, we propose to use a VGG network [58] as the morphology model. A VGG is trained on over a million images [59] to learn a rich set of feature representations. The schematic for the proposed morphology-aware VAE is shown as Fig. 5.

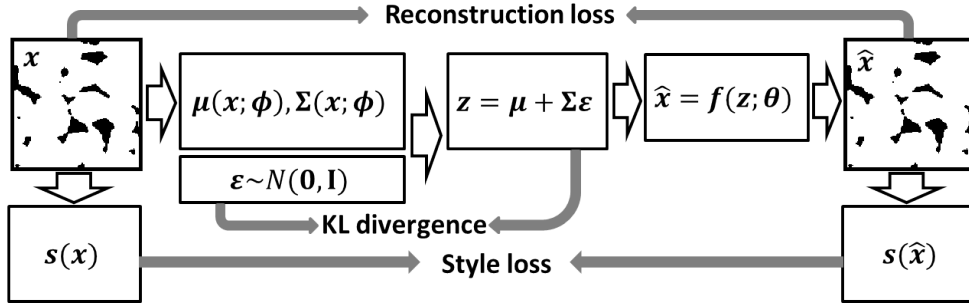


Figure 5: Schematic of the proposed morphology-aware VAE

3.2. Model training

The loss function of the generative model. Training the generative model involves minimizing a loss function with four components:

$$L(\boldsymbol{\theta}, \boldsymbol{\phi}; \mathcal{X}) = L_{\text{RECON}} + L_{\text{KL}} + L_{\text{ST}} + L_{\text{MC}}, \quad (5)$$

where $L_{\text{RECON}} + L_{\text{KL}}$ are the standard reconstruction and KL divergence losses for VAE (see Sec. 2.2), L_{ST} is the style loss, and L_{MC} is an additional loss to prevent mode collapse (introduced below).

The reconstruction loss

$$L_{\text{RECON}} = - \sum_{\mathbf{x}_i \in \mathcal{X}} \mathbb{E}_{q_{\phi}(\mathbf{z}|\mathbf{x}_i)} [\log p_{\boldsymbol{\theta}}(\mathbf{x}_i|\mathbf{z})] \quad (6)$$

measures the reconstruction error of all pairs of authentic microstructures ($\mathbf{x}_i \in \mathcal{X}$) and their reconstructions. The KL divergence loss

$$L_{\text{KL}} = \sum_{\mathbf{x}_i \in \mathcal{X}} D_{\text{KL}}(q_{\phi}(\mathbf{z}|\mathbf{x}_i) || p(\mathbf{z})) \quad (7)$$

measures the difference between the encoder distribution $q_{\phi}(\mathbf{z}|\mathbf{x}_i)$ and the prior $p(\mathbf{z})$. The style loss

$$L_{\text{ST}} = \sum_{s=1}^N \sum_{p=1}^N \sum_l \|\mathbf{G}^{s,l} - \mathbf{G}^{p,l}\|_F^2 \quad (8)$$

measures the total style difference between two sets of N images with indices s and p , representing the generated and the authentic ones, respectively. Given a morphology style model, the Gram matrix $\mathbf{G}^{s,l}$ of image s at the l th hidden layer is defined through elements $G_{i,j}^{s,l} = \sum_k f_{i,k}^{s,l} f_{j,k}^{s,l}$, where feature element $f_{i,k}^{s,l}$ represents the hidden activation corresponding to the i th convolutional filter at spatial location k . $\|\cdot\|_F$ is the Frobenius normal. We note that the definition of feature maps will affect the outcome of style transfer. In general, deeper layers capture styles at larger length scales. We use the first four layers of a standard VGG net. This definition of features is empirical.

Lastly, the mode collapse loss is introduced to prevent the model from producing clustered samples [60], by forcing the generated samples to be different in terms of their activations in the style network. The loss is defined as:

$$L_{\text{MC}} = \frac{2}{N(N-1)} \sum_{i=1}^N \sum_{j=i+1}^N \left(\frac{\mathbf{s}_i^T \mathbf{s}_j}{\|\mathbf{s}_i\| \|\mathbf{s}_j\|} \right)^2, \quad (9)$$

where the style vector \mathbf{s} contains the concatenated and vectorized Gram matrices as defined above.

The training of the generative model. The generative model is trained to minimize the loss defined in Eq. (5) with respect to model parameters $\boldsymbol{\theta}$ and $\boldsymbol{\phi}$ through stochastic gradient descent. To approximate the gradient of the loss, $\nabla_{\boldsymbol{\theta}, \boldsymbol{\phi}}(L_{\text{RECON}} + L_{\text{KL}} + L_{\text{ST}} + L_{\text{MC}})$, we randomly sample 20 authentic material microstructures from \mathcal{X} and generate another 20 artificial microstructures in each training iteration. The artificial microstructures are needed to calculate $\nabla_{\boldsymbol{\theta}, \boldsymbol{\phi}}(L_{\text{ST}} + L_{\text{MC}})$. To prevent neighbouring latent samples to be matched to drastically different style (morphology) targets, we propose to create artificial microstructures by the following procedure: We take each authentic sample \mathbf{x} and pass it through the encoder to get $\boldsymbol{\mu}(\mathbf{x}; \boldsymbol{\phi})$ and $\boldsymbol{\Sigma}(\mathbf{x}; \boldsymbol{\phi})$. We then draw a random sample \mathbf{z} from the latent space following the normal distribution $\mathcal{N}(\mathbf{z} | \boldsymbol{\mu}(\mathbf{x}; \boldsymbol{\phi}), \boldsymbol{\Sigma}(\mathbf{x}; \boldsymbol{\phi}))$, and derive its decoded microstructure $\mathbf{x}' = f(\mathbf{z}; \boldsymbol{\theta})$ to pair with \mathbf{x} . By matching the style of \mathbf{x} and \mathbf{x}' , we ensure that samples close to each other in the latent space will have similar morphologies. We demonstrate the necessity of this treatment in Fig. 6, where we show the generation results from an alternative method where microstructures from a standard normal distribution are randomly paired with the authentic ones for style loss calculation, leading to averaged morphology across all random generations (Fig. 6b). We use Adam optimizer [61] for training, with 200K iterations and a learning rate of 0.001.

The training of the predictive model. We divide the raw data into training, validation, and test sets. The loss function for training the predictive structure-property model is the mean square error of the predicted properties of the training data. Prediction performance of the model on the validation set is monitored to prevent the model from overfitting. The performance of the model is then measured by R-square value of the test data. We use Adam for training with a learning rate of 0.001.

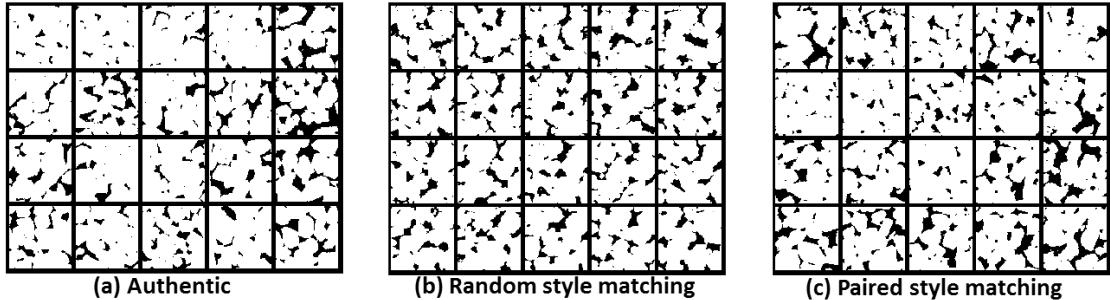


Figure 6: (a) Samples of authentic microstructures (b) Artificial microstructures when random samples are drawn from a standard normal distribution during the training (c) Artificial microstructures when random samples are drawn to pair with the authentic ones

4. Case Study and Results

In this section, we demonstrate key contributions of the proposed model through a case study: (1) By incorporating the style loss, the proposed generative model creates material microstructures with better visual and statistical similarity to the authentic ones than a state-of-the-art Markov random field (MRF) approach; and (2) we can improve the prediction of material properties more effectively by using the artificial data generated from the proposed model than by those generated from a MRF. The case study uses a set of sandstone microstructures and their properties, including Young’s modulus, diffusivity, and fluid permeability. Details of this material system are introduced as follows.

4.1. A case study on the sandstone system

Sandstones are a class of important geological porous materials in petroleum engineering. In the simplest form, a mono-mineral sandstone is composed of a solid (rock) phase and a pore (void) phase, both of which are typically percolating. Extensive research work has been carried out to model the microstructure and physical properties of such porous materials [62, 63, 64, 65, 66, 67, 68, 69, 70, 30]. For example, a fast and independent architecture of artificial neural network has been developed for accurately predicting fluid permeability [71].

We will focus on three different material properties: Young’s modulus (stiffness) E , diffusivity D and fluid permeability k . These properties are respectively sensitive to distinct microstructural features of the materials. In particular, E is mainly determined by the morphology and volume fraction of the rock phase. The diffusivity D is most sensitive to the local pore size distribution. The fluid permeability k depends on the degree of connectivity of the pore phase as well as the pore/rock interface morphology. Thus, successfully improving the prediction accuracy for all three material properties poses a stringent test for our morphology-aware generative model for effectively populating the microstructure sample space.

Physics-based material property calculations. The material properties used to train the network model are first computed using the effective medium theory [8]. The Young’s modulus

can be written as

$$E = \frac{9K_e G_e}{3K_e + G_e}, \quad (10)$$

where K_e and G_e are respectively the bulk and shear modulus of the materials. We use analytical approximations of K_e and G_e obtained by truncating the associated strong-contrast expansions after the third order term [72], which are respectively given by

$$\phi_2 \frac{\kappa_{21}}{\kappa_{e1}} = 1 - \frac{(d+2)(d-1)G_1 \kappa_{21} \mu_{21}}{d(K_1 + 2G_1)} \phi_1 \chi \quad (11)$$

and

$$\phi_2 \frac{\mu_{21}}{\mu_{e1}} = 1 - \frac{2G_1 \kappa_{21} \mu_{21}}{d(K_1 + G_1)} \phi_1 \chi - \frac{2G_1 \kappa_{21} \mu_{21}}{d(K_1 + 2G_1)} \phi_1 \chi - \frac{1}{2d} \left[\frac{dK_1 + (d-2)G_1}{K_1 + 2G_1} \right]^2 \mu_{21}^2 \phi_1 \eta_2, \quad (12)$$

where ϕ_1 and ϕ_2 are respectively the volume fraction of the rock phase and void phase (i.e., porosity); d is the spatial dimension of the material system; K_p and G_p are respectively the bulk and shear modulus of phase p ; and the scalar parameters κ_{pq} and μ_{pq} ($p, q = 1, 2, e$) are respectively the bulk and shear modulus polarizability, i.e.,

$$\kappa_{pq} = \frac{K_p - K_q}{K_q + \frac{2(d-1)}{d} G_q} \quad (13)$$

and

$$\mu_{pq} = \frac{G_p - G_q}{G_q} \frac{1}{1 + \frac{\frac{d}{2} K_q + \frac{(d+1)(d-2)}{d} G_1}{K_q + 2G_q}}. \quad (14)$$

The quantities χ and η_2 are the microstructural parameters associated with the void (pore) phase involving the three-point correlation functions S_3 and two-point correlation functions S_2 of the pore phase, i.e.,

$$\chi = \frac{9}{2\phi_1 \phi_2} \int_0^\infty \frac{dr}{r} \int_0^\infty \frac{ds}{s} \int_{-1}^1 d(\cos \theta) P_2(\cos \theta) [S_3(r, s, t) - \frac{S_2(r)S_2(t)}{\phi_2}] \quad (15)$$

and

$$\eta_2 = \frac{5}{21} \chi + \frac{150}{7\phi_1 \phi_2} \int_0^\infty \frac{dr}{r} \int_0^\infty \frac{ds}{s} \int_{-1}^1 d(\cos \theta) P_4(\cos \theta) [S_3(r, s, t) - \frac{S_2(r)S_2(t)}{\phi_2}], \quad (16)$$

where $t = (r^2 + s^2 - 2rs \cos \theta)^{1/2}$, and P_2 and P_4 are respectively the Legendre polynomials of order two and four, i.e.,

$$P_2(x) = \frac{1}{2}(3x^2 - 1), \quad P_4(x) = \frac{1}{8}(35x^4 - 30x^2 + 3). \quad (17)$$

In our system, the void phase possesses zero elastic moduli, i.e., $K_2 = G_2 = 0$, and the moduli of the rock phase are respectively $K_1 = 4.3$ GPa and $G_2 = 3.8$ GPa. The three-point

parameters χ and η_2 are computed by first evaluating the correlation functions S_3 and S_2 of the void phase from the microstructure data and then evaluating the integrals. In the reported results, the overall Young’s modulus of the sandstone is re-scaled with respect to that of the rock phase.

Similar to the elastic moduli, we use an analytical approximation [73, 74] obtained by truncating the strong-contrast expansion of the effective diffusion coefficient D after the third order term:

$$\frac{D}{D_2} = \frac{1 + 2\phi_1\beta_{12} - 2\phi_2\chi\beta_{12}^2}{1 - \phi_1\beta_{12} - 2\phi_2\chi\beta_{12}^2}, \quad (18)$$

where ϕ_1 and ϕ_2 are respectively the volume fraction of the rock and pore phases. The polarization parameter β_{12} is given by

$$\beta_{12} = \frac{D_2 - D_1}{D_2 + 2D_1}, \quad (19)$$

where D_1 and D_2 are respectively the diffusivity of the rock and pore phases. In our sandstone system, the rock diffusivity is typically negligibly small compared with the pore phase diffusivity, and thus $D_1/D_2 \approx 0$. The three-point parameter χ for the rock phase is given by Eq. (15), in which the correlation function S_3 and S_2 are computed from the microstructural data for the rock phase (instead of the pore phase as in the case of elastic moduli). The computed D values are normalized with respect to D_2 in the reported data.

Finally, the fluid permeability is computed using the approximation [75]

$$k = \frac{2}{3(1 - \phi_2)^2} \int_0^\infty [S_2(r) - \phi_2^2] r dr, \quad (20)$$

where ϕ_2 is the volume fraction of the pore phase and S_2 is the associated two-point correlation function.

4.2. Results

The effect of style loss on material generation. In Fig. 7, we show that a standard VAE has undesirable generation performance with a small training set (200 samples), and that the incorporation of the style loss can effectively improve the generation quality under the same sample size. Further, the proposed approach also produces more plausible microstructures than the MRF method [35], as one can observe the scattering of unrealistically small particles of the “stone” phase from the latter.

Structure-property predictions. Here we investigate how the prediction accuracy of a structure-property model improves with the additional training data, acquired through the proposed method and the MRF. To do so, we start by deriving baseline models (for all three structure-property mappings) using 100 data points for training and another 100 for validation. The baseline prediction performance is evaluated using a third set of 100 test data points. The true property values are calculated following Sec. 4.1, and normalized for training.

Two sets of artificial microstructures, 1000 samples each, are created using the proposed method and the MRF, respectively. The true properties of these samples are computed.

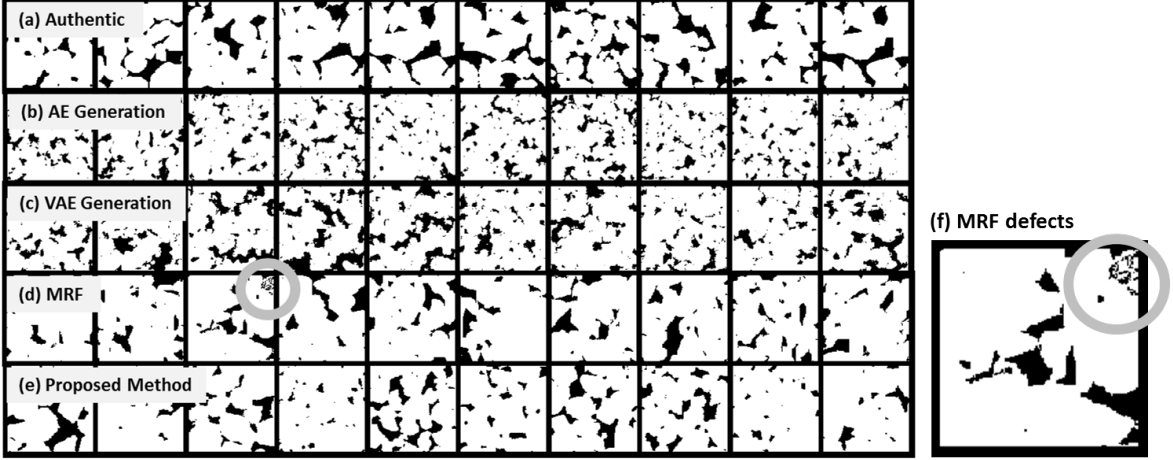


Figure 7: (a) The authentic sandstone microstructure samples (b) Generations from a standard autoencoder (c) Generations from a standard VAE (d) Generations from the MRF method in [35] (e) Generations from the proposed method (f) An enlarged example of MRF generation with artificial defects

We then use these additional samples to improve the performance of the predictive models. Specifically, an increasing number of additional data points (from 50 to 1000) from the two sets are randomly added to the original training set to update the predictive model. We perform 10 independent random draws for each size of the additional data, and report the means and variances of the resultant test R-squares. The exception is with data size 1000, where all data points are used all together.

Results are presented in Fig. 8 and summarized as follows. (1) Microstructures generated from the proposed method have property distributions similar to those of the authentic samples, while those generated from MRF have significantly smaller variances (Fig. 8a). While the MRF method ensures variance in the microstructure space, as is evident from Fig. 7, the lack of variance in the volume fraction of its generations may cause the observed small variances in the properties. It is worth noting that while a modified MRF approach that considers variance in volume fraction may improve its generation quality, our approach does not require human identification or design of such features, as variances in morphology are directly learned through the generative model. (2) The statistical difference in properties observed in (1) may explain the significant gap in the prediction performance of the resultant structure-property models, as seen in Fig. 8b. The narrow distribution of properties of the MRF method also explains the drop in model performance from 800 to 1000 samples: By feeding the network data from one distribution while asking it to predict on those drawn from another, we may encounter deteriorated performance even with an increased training data size.

5. Discussion

Utilities of the proposed method. The proposed generative model captures low-dimensional representations of data points distributed in high-dimensional spaces. The model can be

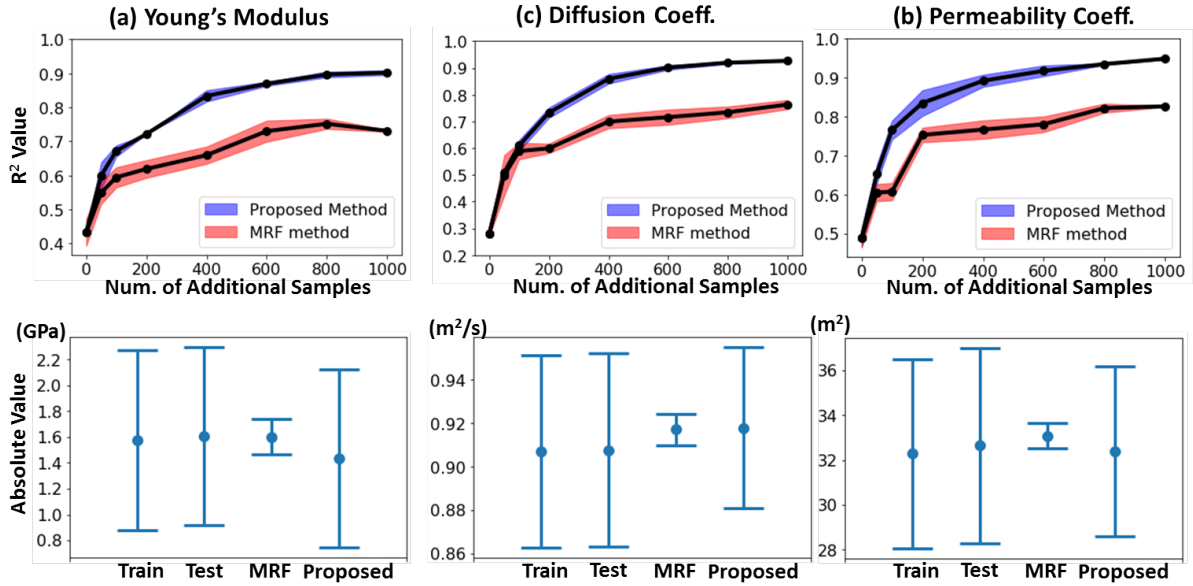


Figure 8: (a) Property distributions of microstructures generated from the proposed and the MRF [35] models. (b) Test R-square values at an increasing number of additional data points

used to facilitate more cost-effective design of optimal and feasible microstructures by providing extra data to improve predictive structure-property models. This value could be particularly significant when the bottleneck of the design task is the high acquisition cost of microstructure data. It is also worth noting that the model may also help to reduce the cost of structure-property mappings, through its identification of low-dimensional material representations. For example, during the training of a predictive structure-property model, one may adopt an active learning strategy to only sample microstructures with high uncertainties in their property predictions, thus improving the predictive model cost-effectively. The model and the learning algorithm are also generally applicable, as they are independent from any specific material system, except that minor model architecture tuning may be needed to incorporate different morphological complexities.

5.1. Physics-based generative model

The successful application of style loss in this paper inspires future investigation on whether physics-based loss can be applied to further improve the quality of microstructure generations through a generative model with limited data. Specifically, instead of using a style loss, we can measure the similarity between input and output microstructures based on their properties. For example, for microstructures that satisfy certain equilibrium conditions (governed by the underlying process-structure mapping), we can train the generative model to minimize the violation of these conditions, and thus enforcing the artificial samples to be physically meaningful.

6. Conclusions

This paper proposed a method for generating an arbitrary amount of artificial microstructure samples with low computation cost and a small amount of training samples. The key contribution is the incorporation of a style loss into the training to significantly improve the quality of the artificial microstructures. For verification, we applied the proposed method to generating sandstone samples. Results showed that our method is more data-efficient at improving the prediction performance of a structure-property mapping than a state-of-the-art Markov Random Field method. The findings from this paper inspired future investigation into physically meaningful generative models for accelerating microstructure-mediated material design.

References

- [1] A. Jain, S. P. Ong, G. Hautier, W. Chen, W. D. Richards, S. Dacek, S. Cholia, D. Gunter, D. Skinner, G. Ceder, et al., Commentary: The materials project: A materials genome approach to accelerating materials innovation, *Apl Materials* 1 (1) (2013) 011002.
- [2] G. Hautier, C. Fischer, V. Ehrlacher, A. Jain, G. Ceder, Data mined ionic substitutions for the discovery of new compounds, *Inorganic chemistry* 50 (2) (2010) 656–663.
- [3] R. Kondo, S. Yamakawa, Y. Masuoka, S. Tajima, R. Asahi, Microstructure recognition using convolutional neural networks for prediction of ionic conductivity in ceramics, *Acta Materialia*.
- [4] T. D. Huan, A. Mannodi-Kanakkithodi, C. Kim, V. Sharma, G. Pilania, R. Ramprasad, A polymer dataset for accelerated property prediction and design, *Scientific data* 3.
- [5] D. P. Kingma, M. Welling, Auto-encoding variational bayes, in: Proceedings of the 2nd International Conference on Learning Representations, Arizona, US, ICLR, 2013.
- [6] L. A. Gatys, A. S. Ecker, M. Bethge, Image style transfer using convolutional neural networks, in: Proceedings of the IEEE Conference on Computer Vision and Pattern Recognition, 2016, pp. 2414–2423.
- [7] S. Curtarolo, G. L. Hart, M. B. Nardelli, N. Mingo, S. Sanvito, O. Levy, The high-throughput highway to computational materials design, *Nature materials* 12 (3) (2013) 191–201.
- [8] S. Torquato, *Random heterogeneous materials: microstructure and macroscopic properties*, Vol. 16, Springer Science & Business Media, New York, US, 2013.
- [9] Z. Jiang, W. Chen, C. Burkhardt, Efficient 3D porous microstructure reconstruction via gaussian random field and hybrid optimization, *Journal of microscopy* 252 (2) (2013) 135–148.
- [10] M. Grigoriu, Random field models for two-phase microstructures, *Journal of Applied Physics* 94 (6) (2003) 3762–3770.
- [11] H. Xu, D. A. Dikin, C. Burkhardt, W. Chen, Descriptor-based methodology for statistical characterization and 3D reconstruction of microstructural materials, *Computational Materials Science* 85 (2014) 206–216.
- [12] S. Yu, Y. Zhang, C. Wang, W.-k. Lee, B. Dong, T. W. Odom, C. Sun, W. Chen, Characterization and design of functional quasi-random nanostructured materials using spectral density function, *Journal of Mechanical Design* 139 (7) (2017) 071401.
- [13] S. Broderick, C. Suh, J. Nowers, B. Vogel, S. Mallapragada, B. Narasimhan, K. Rajan, Informatics for combinatorial materials science, *JOM Journal of the Minerals, Metals and Materials Society* 60 (3) (2008) 56–59.
- [14] M. F. Ashby, Materials selection in mechanical design, *MRS Bull* 30 (12) (2005) 995.
- [15] M. Steinzig, F. Harlow, Probability distribution function evolution for binary alloy solidification, in: *Solidification*, Proceedings of the Minerals, Metals, Materials Society Annual Meeting, San Diego, CA, Citeseer, 1999, pp. 197–206.

- [16] A. Tewari, A. Gokhale, Nearest-neighbor distances between particles of finite size in three-dimensional uniform random microstructures, *Materials Science and Engineering: A* 385 (1) (2004) 332–341.
- [17] A. D. Rollett, S.-B. Lee, R. Campman, G. Rohrer, Three-dimensional characterization of microstructure by electron back-scatter diffraction, *Annu. Rev. Mater. Res.* 37 (2007) 627–658.
- [18] A. Borbely, F. Csikor, S. Zabler, P. Cloetens, H. Biermann, Three-dimensional characterization of the microstructure of a metal–matrix composite by holotomography, *Materials Science and Engineering: A* 367 (1) (2004) 40–50.
- [19] R. Pytz, *Microstructure description of composites, statistical methods, mechanics of microstructure materials*, CISM Courses and Lectures.
- [20] J. Scalon, N. Fieller, E. Stillman, H. Atkinson, Spatial pattern analysis of second-phase particles in composite materials, *Materials Science and Engineering: A* 356 (1) (2003) 245–257.
- [21] V. Sundararaghavan, N. Zabaras, Classification and reconstruction of three-dimensional microstructures using support vector machines, *Computational Materials Science* 32 (2) (2005) 223–239.
- [22] D. Basanta, M. A. Miodownik, E. A. Holm, P. J. Bentley, Using genetic algorithms to evolve three-dimensional microstructures from two-dimensional micrographs, *Metallurgical and Materials Transactions A* 36 (7) (2005) 1643–1652.
- [23] S. Holotescu, F. Stoian, Prediction of particle size distribution effects on thermal conductivity of particulate composites, *Materialwissenschaft Und Werkstofftechnik* 42 (5) (2011) 379–385.
- [24] C. Klaysom, S.-H. Moon, B. P. Ladewig, G. M. Lu, L. Wang, The effects of aspect ratio of inorganic fillers on the structure and property of composite ion-exchange membranes, *Journal of colloid and interface science* 363 (2) (2011) 431–439.
- [25] J. Gruber, A. Rollett, G. Rohrer, Misorientation texture development during grain growth. Part II: Theory, *Acta Materialia* 58 (1) (2010) 14–19.
- [26] Y. Liu, M. S. Greene, W. Chen, D. A. Dikin, W. K. Liu, Computational microstructure characterization and reconstruction for stochastic multiscale material design, *Computer-Aided Design* 45 (1) (2013) 65–76.
- [27] M. D. Rintoul, S. Torquato, Reconstruction of the structure of dispersions, *Journal of Colloid and Interface Science* 186 (2) (1997) 467–476.
- [28] C. Yeong, S. Torquato, Reconstructing random media, *Physical Review E* 57 (1) (1998) 495.
- [29] H. Okabe, M. J. Blunt, Pore space reconstruction using multiple-point statistics, *Journal of Petroleum Science and Engineering* 46 (1) (2005) 121–137.
- [30] A. Hajizadeh, A. Safekordi, F. A. Farhadpour, A multiple-point statistics algorithm for 3D pore space reconstruction from 2D images, *Advances in water Resources* 34 (10) (2011) 1256–1267.
- [31] P.-E. Øren, S. Bakke, Reconstruction of berea sandstone and pore-scale modelling of wettability effects, *Journal of Petroleum Science and Engineering* 39 (3) (2003) 177–199.
- [32] D. Fullwood, S. Kalidindi, S. Niezgod, A. Fast, N. Hampson, Gradient-based microstructure reconstructions from distributions using fast fourier transforms, *Materials Science and Engineering: A* 494 (1) (2008) 68–72.
- [33] D. T. Fullwood, S. R. Niezgod, S. R. Kalidindi, Microstructure reconstructions from 2-point statistics using phase-recovery algorithms, *Acta Materialia* 56 (5) (2008) 942–948.
- [34] A. P. Roberts, Statistical reconstruction of three-dimensional porous media from two-dimensional images, *Physical Review E* 56 (3) (1997) 3203.
- [35] R. Bostanabad, A. T. Bui, W. Xie, D. W. Apley, W. Chen, Stochastic microstructure characterization and reconstruction via supervised learning, *Acta Materialia* 103 (2016) 89–102.
- [36] X. Liu, V. Shapiro, Random heterogeneous materials via texture synthesis, *Computational Materials Science* 99 (2015) 177–189.
- [37] J. A. Quiblier, A new three-dimensional modeling technique for studying porous media, *Journal of Colloid and Interface Science* 98 (1) (1984) 84–102.
- [38] M. Ostoj, Random field models of heterogeneous materials, *International Journal of Solids and Structures* 35 (19) (1998) 2429–2455.
- [39] Y. Jiao, F. Stillinger, S. Torquato, Modeling heterogeneous materials via two-point correlation func-

- tions. ii. algorithmic details and applications, *Physical Review E* 77 (3) (2008) 031135.
- [40] Y. Jiao, F. Stillinger, S. Torquato, A superior descriptor of random textures and its predictive capacity, *Proceedings of the National Academy of Sciences* 106 (42) (2009) 17634–17639.
- [41] M. V. Karsanina, K. M. Gerke, E. B. Skvortsova, D. Mallants, Universal spatial correlation functions for describing and reconstructing soil microstructure, *PloS one* 10 (5) (2015) e0126515.
- [42] R. Cang, Y. Xu, S. Chen, Y. Liu, Y. Jiao, M. Y. Ren, Microstructure representation and reconstruction of heterogeneous materials via deep belief network for computational material design, *Journal of Mechanical Design* 139 (7) (2017) 071404.
- [43] R. Cang, A. Vipradas, Y. Ren, Scalable microstructure reconstruction with multi-scale pattern preservation, in: *ASME 2017 International Design Engineering Technical Conferences and Computers and Information in Engineering Conference*, American Society of Mechanical Engineers, 2017, pp. V02BT03A010–V02BT03A010.
- [44] H. Lee, R. Grosse, R. Ranganath, A. Y. Ng, Convolutional deep belief networks for scalable unsupervised learning of hierarchical representations, in: *Proceedings of the 26th annual international conference on machine learning*, ACM, 2009, pp. 609–616.
- [45] S. Tong, E. Chang, Support vector machine active learning for image retrieval, in: *Proceedings of the ninth ACM international conference on Multimedia*, ACM, 2001, pp. 107–118.
- [46] B. Settles, Active learning literature survey, *University of Wisconsin, Madison* 52 (55-66) (2010) 11.
- [47] J. Ling, M. Hutchinson, E. Antono, S. Paradiso, B. Meredig, High-dimensional materials and process optimization using data-driven experimental design with well-calibrated uncertainty estimates, *arXiv preprint arXiv:1704.07423*.
- [48] T. Lookman, F. J. Alexander, A. R. Bishop, Perspective: Codesign for materials science: An optimal learning approach, *APL Materials* 4 (5) (2016) 053501.
- [49] Y. Bengio, et al., Learning deep architectures for ai, *Foundations and trends® in Machine Learning* 2 (1) (2009) 1–127.
- [50] A. Ng, Sparse autoencoder, *CS294A Lecture notes* 72 (2011) (2011) 1–19.
- [51] P. Vincent, H. Larochelle, Y. Bengio, P.-A. Manzagol, Extracting and composing robust features with denoising autoencoders, in: *Proceedings of the 25th international conference on Machine learning*, ACM, 2008, pp. 1096–1103.
- [52] S. Rifai, P. Vincent, X. Muller, X. Glorot, Y. Bengio, Contractive auto-encoders: Explicit invariance during feature extraction, in: *Proceedings of the 28th international conference on machine learning (ICML-11)*, 2011, pp. 833–840.
- [53] Q. V. Le, et al., A tutorial on deep learning part 2: Autoencoders, convolutional neural networks and recurrent neural networks, *Google Brain*.
- [54] Y. Bengio, P. Lamblin, D. Popovici, H. Larochelle, Greedy layer-wise training of deep networks, in: *Advances in neural information processing systems*, 2007, pp. 153–160.
- [55] C. Xing, L. Ma, X. Yang, Stacked denoise autoencoder based feature extraction and classification for hyperspectral images, *Journal of Sensors* 2016.
- [56] C. Szegedy, W. Liu, Y. Jia, P. Sermanet, S. Reed, D. Anguelov, D. Erhan, V. Vanhoucke, A. Rabinovich, Going deeper with convolutions, in: *Proceedings of the IEEE conference on computer vision and pattern recognition*, 2015, pp. 1–9.
- [57] K. Simonyan, A. Zisserman, Very deep convolutional networks for large-scale image recognition, *arXiv preprint arXiv:1409.1556*.
- [58] K. Simonyan, A. Zisserman, Very deep convolutional networks for large-scale image recognition, *CoRR abs/1409.1556*.
- [59] J. Deng, W. Dong, R. Socher, L.-J. Li, K. Li, L. Fei-Fei, ImageNet: A Large-Scale Hierarchical Image Database, in: *CVPR09*, 2009.
- [60] J. Zhao, M. Mathieu, Y. LeCun, Energy-based generative adversarial network, *arXiv preprint arXiv:1609.03126*.
- [61] D. Kingma, J. Ba, Adam: A method for stochastic optimization, *arXiv preprint arXiv:1412.6980*.
- [62] M. Sahimi, Flow and transport in porous media and fractured rock: from classical methods to modern

- approaches, John Wiley & Sons, 2011.
- [63] A. Radlinski, M. Ioannidis, A. Hinde, M. Hainbuchner, M. Baron, H. Rauch, S. Kline, Angstrom-to-millimeter characterization of sedimentary rock microstructure, *Journal of colloid and interface science* 274 (2) (2004) 607–612.
 - [64] K. L. Milliken, S. E. Laubach, Brittle deformation in sandstone diagenesis as revealed by scanned cathodoluminescence imaging with application to characterization of fractured reservoirs, in: *Cathodoluminescence in geosciences*, Springer, 2000, pp. 225–243.
 - [65] S. C. Blair, P. A. Berge, J. G. Berryman, Using two-point correlation functions to characterize microgeometry and estimate permeabilities of sandstones and porous glass, *Journal of Geophysical Research: Solid Earth* 101 (B9) (1996) 20359–20375.
 - [66] D. A. Coker, S. Torquato, J. H. Dunsmuir, Morphology and physical properties of fontainebleau sandstone via a tomographic analysis, *Journal of Geophysical Research: Solid Earth* 101 (B8) (1996) 17497–17506.
 - [67] M. Antonellini, A. Aydin, D. Pollard, P. d’Onfro, Petrophysical study of faults in sandstone using petrographic image analysis and x-ray computerized tomography, *Pure and Applied Geophysics* 143 (1-3) (1994) 181–201.
 - [68] R. Al-Raoush, C. Willson, Extraction of physically realistic pore network properties from three-dimensional synchrotron x-ray microtomography images of unconsolidated porous media systems, *Journal of hydrology* 300 (1) (2005) 44–64.
 - [69] C. R. Appoloni, Á. Macedo, C. P. Fernandes, P. C. Philippi, Characterization of porous microstructure by x-ray microtomography, *X-Ray Spectrometry* 31 (2) (2002) 124–127.
 - [70] H. Li, P.-E. Chen, Y. Jiao, Accurate reconstruction of porous materials via stochastic fusion of limited bimodal microstructural data, *Transport in Porous Media* (2017) 1–18.
 - [71] P. Tahmasebi, A. Hezarkhani, A fast and independent architecture of artificial neural network for permeability prediction, *Journal of Petroleum Science and Engineering* 86 (2012) 118–126.
 - [72] S. Torquato, Exact expression for the effective elastic tensor of disordered composites, *Physical review letters* 79 (4) (1997) 681.
 - [73] S. Torquato, Effective electrical conductivity of two-phase disordered composite media, *Journal of Applied Physics* 58 (10) (1985) 3790–3797.
 - [74] Y. Jiao, S. Torquato, Quantitative characterization of the microstructure and transport properties of biopolymer networks, *Physical biology* 9 (3) (2012) 036009.
 - [75] S. Torquato, B. Lu, Rigorous bounds on the fluid permeability: effect of polydispersivity in grain size, *Physics of Fluids A: Fluid Dynamics* 2 (4) (1990) 487–490.